Journal of Neural Engineering

PAPER

Optimal artifact suppression in simultaneous electrocorticography stimulation and recording for bi-directional brain-computer interface applications

To cite this article: Haoran Pu *et al* 2020 *J. Neural Eng.* **17** 026038

IOP Publishing J. Neural Eng. **17** (2020) 026038 https://doi.org/10.1088/1741-2552/ab82ac

Journal of Neural Engineering

RECEIVED
26 October 2019

REVISED
15 February 2020

ACCEPTED FOR PUBLICATION
24 March 2020

PUBLISHED
28 April 2020

PAPER

Optimal artifact suppression in simultaneous electrocorticography stimulation and recording for bi-directional brain-computer interface applications

Haoran Pu[1], **Jeffrey Lim**[2], **Spencer Kellis**[4], **Charles Y Liu**[3], **Richard A Andersen**[4], **An H Do**[5], **Payam Heydari**[1] **and Zoran Nenadic**[1,2]

[1] Department of Electrical Engineering and Computer Science, University of California, Irvine, Irvine, CA, 92697, United States of America
[2] Department of Biomedical Engineering, University of California, Irvine, Irvine, CA, 92697, United States of America
[3] Department of Neurological Surgery, University of Southern California, Los Angeles, CA, 90033, United States of America
[4] Division of Biology and Biological Engineering, California Institute of Technology, Pasadena, CA, 91125, United States of America
[5] Department of Neurology, University of California Irvine, Irvine, CA, 92697, United States of America

E-mail: **haoranp1@uci.edu** **and** **znenadic@uci.edu**

Keywords: electrocorticography, bi-directional brain-computer interfaces, artifact suppression, optimization, dipole model

Supplementary material for this article is available online

Abstract

Objective. Electrocorticogram (ECoG)-based brain-computer interfaces (BCIs) are a promising platform for the restoration of motor and sensory functions to those with neurological deficits. Such bi-directional BCI operation necessitates simultaneous ECoG recording and stimulation, which is challenging given the presence of strong stimulation artifacts. This problem is exacerbated if the BCI's analog front-end operates in an ultra-low power regime, which is a basic requirement for fully implantable medical devices. In this study, we developed a novel method for the suppression of stimulation artifacts before they reach the analog front-end. *Approach.* Using elementary biophysical considerations, we devised an artifact suppression method that employs a weak auxiliary stimulation delivered between the primary stimulator and the recording grid. The exact location and amplitude of this auxiliary stimulating dipole were then found through a constrained optimization procedure. The performance of our method was tested in both simulations and phantom brain tissue experiments. *Main results.* The solution found through the optimization procedure matched the optimal canceling dipole in both simulations and experiments. Artifact suppression as large as 28.7 dB and 22.9 dB were achieved in simulations and brain phantom experiments, respectively. *Significance.* We developed a simple constrained optimization-based method for finding the parameters of an auxiliary stimulating dipole that yields optimal artifact suppression. Our method suppresses stimulation artifacts before they reach the analog front-end and may prevent the front-end amplifiers from saturation. Additionally, it can be used along with other artifact mitigation techniques to further reduce stimulation artifacts.

1. Introduction

Most people living with chronic spinal cord injury (SCI) are affected by impairment of sensory and motor functions below the level of injury. Brain-computer interfaces (BCIs) may be a promising approach to addressing SCI and many other neurological conditions [1]. Subdurally recorded electrocorticogram (ECoG) is a suitable signal platform for BCI applications because ECoG electrode grids are not as invasive as intracortical microelectrode arrays, yet their spatio-temporal resolution, signal-to-noise ratio (SNR), and susceptibility to artifacts are far superior to those of electroencephalogram (EEG) [2]. Recent studies showed promising results in using ECoG-based BCIs to restore motor functions to those with severe paralysis [3, 4]. However, these BCI systems exclusively relied on visual feedback. Therefore, their performance was arguably suboptimal due to the lack of proprioceptive and tactile feedback. Since these percepts can be elicited by ECoG electrostimulation [5, 6], it can be envisioned that sensory information will be integrated into future ECoG-based BCIs. These bi-directional (BD)-BCIs will have the capability to concurrently restore motor and sensory functions in a biomimetic manner.

Unlike similar bi-directional brain interfaces, such as responsive neurostimulators (RNSs) [7], where simultaneous recording and stimulation are not necessary, BD-BCIs for movement restoration must decode movement intentions while simultaneously eliciting artificial sensation. Simultaneous recording and stimulation in this fashion poses a significant challenge due to the presence of extremely strong stimulation artifacts [8]. For example, given a typical electrode-tissue impedance of 1 kΩ [9] and sensation-eliciting stimulating current of 5 mA [5], the stimulation voltage of 5 V may be necessary. In contrast, recorded ECoG signals have substantially smaller amplitudes ($<$100 μV [2]). To mitigate this problem, various artifact suppression techniques have been proposed [10], ranging from those focused on analog front-ends [11, 12] to digital filtering [11, 13, 14]. However, these approaches would fail if the amplifiers were saturated by extremely strong artifacts, and no amount of signal processing could recover neural signals of interest. Amplifier saturation is even more likely for analog front-ends operating in an ultra-low power (ULP) regime, which is a basic requirement for fully implantable BCIs. This issue thus necessitates a solution that works at the front-end in order to prevent saturation and preserve the recording.

Recently, we introduced an artifact cancellation technique [15], where the stimulation artifacts were reduced by introducing weak canceling currents via ECoG electrodes located between the primary stimulator and the recording electrodes. The major advantage of this approach is that it suppresses artifacts *before* they reach recording electrodes while minimally increasing the stimulation power overhead. Although successful, this proof-of-concept study used canceling patterns that were chosen heuristically. In contrast, this study exploits insights from volume conduction theory and casts the artifact cancellation problem within a mathematical framework [15]. Specifically, we formulate artifact cancellation as an optimization problem, wherein the effect of stimulation artifacts on the recording side is minimized, while satisfying physical and physiological constraints. The optimal canceling patterns produced by our method have been successfully validated both in simulations and brain phantom tissue experiments. If successfully tested in humans, our method may offer a promising solution to subdural artifact cancellation which could be widely adopted in future ECoG-based BD-BCI systems.

2. Methods

2.1. Artifact cancellation by auxiliary stimulation

Our approach exploits the primarily resistive volume conduction nature of the brain. Namely, at frequencies below 10 kHz, the brain tissue largely behaves as a bulk resistive medium [16–19]. While the electrode-tissue interface has non-negligible capacitive effects and, thus, may introduce phase lags, we previously found a consistently tight phase-locking of stimulation artifacts across spatially distributed ECoG electrodes [20, 21]. This observation suggests that, despite the heterogeneous composition of neural tissue and capacitive effects of electrode-tissue interface, the spatial distribution of artifacts can be accurately described by a resistive model, such as a dipole [15, 20, 21]. The artifact potential field could then be controlled by placing an auxiliary stimulation dipole of the opposite polarity nearby.

This concept is best demonstrated using a simple monopole model, as shown in figure 1. After introducing an auxiliary stimulating (canceling) current between the primary stimulation site and the recording region, the net artifact falls below a hypothetical analog front-end saturation voltage across the entire recording region.

To further advance this idea, we note that the potential field generated by a bipolar charge-balanced ECoG stimulation (a standard clinical practice) can be described by a dipole model (see appendix A for details). Our preliminary study [15] provides empirical evidence for this idea and shows that the addition of an auxiliary dipole produces a cancellation effect that reduces the amplitude of artifacts. However, choosing the location and intensity of the canceling dipole heuristically can hardly guarantee optimal artifact suppression performance. Therefore, this study proposes to find these parameters through an optimization procedure.

2.2. Proposed optimization framework

To minimize the worst case artifacts across the recording grid, the optimal canceling pattern (canceling dipole locations and canceling currents) must be found through an optimization process. Additionally, such an optimal canceling pattern must satisfy several physical and physiological constraints. These constraints are defined as binary variables (0 when the constraints are satisfied, 1 otherwise). First, a canceling dipole physical constraint (PC) is introduced to prevent primary and/or canceling dipole overlap. Second, the canceling dipoles may cause unwanted sensation if their currents are too large. To address this issue, a local sensation constraint (SC) is defined to restrict the canceling currents to a threshold. Third, the voltages created by canceling dipoles can potentially counteract the voltage induced by the primary stimulating dipole and cause a loss in sensation. Therefore, an interference constraint (IC) is introduced to impose a restriction on the voltage induced by the canceling dipoles. Formally, the artifact cancellation problem can be cast as the following constrained optimization problem:

$$\boldsymbol{os} = \underset{\boldsymbol{cs}}{\operatorname{argmin}}\, F(\boldsymbol{cs}) \quad \text{subject to} \quad PC + SC + IC = 0 \tag{1}$$

where $\boldsymbol{cs}$ is a candidate solution, $\boldsymbol{os}$ is the optimal solution (see appendix B for details) and $F(\boldsymbol{cs})$ is the objective function. Specifically, $F(\boldsymbol{cs})$ is defined as the maximum net voltage observed by the recording grid (details in section 2.2.1). Variables to be optimized are canceling dipole locations and currents (parametrized by β, where $\beta \in [0,1]$ is the amplitude ratio of the auxiliary and primary stimulating currents). The optimization algorithm iteratively inspects all the candidate solutions, and determines whether they satisfy the three constraints. Based on the optimization algorithm, a mathematical model is constructed accordingly to characterize concurrent ECoG stimulation and recording as well as incorporate cancellation (see appendix C for details). The pseudo-code for the optimization framework is shown in algorithm 1 with all the notations defined in table 1.

Algorithm 1 Iterative approach to find canceling pattern with the minimum amount of artifacts.

```
Require: $MP$
  Generate $A$ from $MP$
  $\boldsymbol{os} \leftarrow$ Randomly choose a candidate solution in $A$
  $A \leftarrow A \setminus \{\boldsymbol{os}\}$
  while $A \neq \varnothing$ do
    $\boldsymbol{cs} \leftarrow$ Randomly choose a candidate solution in $A$
    if $F(\boldsymbol{cs}) \leq F(\boldsymbol{os})$ then
      Update $PC, SC, IC$
      if $PC + SC + IC = 0$ then
        $\boldsymbol{os} \leftarrow \boldsymbol{cs}$
      end if
    end if
    $A \leftarrow A \setminus \{\boldsymbol{cs}\}$
  end while
  return $\boldsymbol{os}$
```

We elaborate on the optimization framework in subsequent sub-sections.

2.2.1. Objective function $F(\boldsymbol{cs})$

To explicitly demonstrate all the variables to be optimized in the candidate solution ($\boldsymbol{cs}$), we define $P_{\mathrm{t}}(\hat{x}_{\mathrm{r}}, \hat{y}_{\mathrm{r}}, \boldsymbol{cs})$ as the net voltage amplitude at a recording electrode location $(\hat{x}_{\mathrm{r}}, \hat{y}_{\mathrm{r}})$ (by substituting equation (C4) and (C5) into equation (A5)), i.e.

$$P_{\mathrm{t}}(\hat{x}_{\mathrm{r}}, \hat{y}_{\mathrm{r}}, \boldsymbol{cs}) = V_{\mathrm{t}}(\hat{x}_{\mathrm{r}}, \hat{y}_{\mathrm{r}}) \tag{2}$$

Accordingly, we define the objective function to represent the largest net artifact over all possible recording electrode locations, i.e.

$$F(\boldsymbol{cs}) = \max_{p_{\mathrm{r}}, q_{\mathrm{r}}} |P_{\mathrm{t}}(\hat{x}_{\mathrm{r}}, \hat{y}_{\mathrm{r}}, \boldsymbol{cs})| \tag{3}$$

where $p_r = 0, 1, \ldots, X_r - 1$, $q_r = 0, 1, \ldots, Y_r - 1$, and X_r and Y_r are the number of rows and columns in the recording grid, respectively (see appendix C).

2.2.2. Canceling dipole physical constraint (PC)

PC excludes the candidate solution(s) based on two sub-constraints (see appendix D for details). The first sub-constraint excludes cases wherein one or more canceling electrodes overlap with the primary stimulating electrodes. The second sub-constraint leaves out candidate solution(s) with two or more canceling dipoles sharing electrodes. The reason for this exclusion is that overlapped electrodes can ruin the dipolar structure of the canceling currents, which may cause difficulties in practical implementation. On the other hand, if two canceling dipoles fully overlap, this solution is redundant and can be recreated by decreasing the number of canceling dipoles, N, (see appendix C).

2.2.3. Local sensation constraint (SC)

Assuming the primary stimulation meets all the FDA safety requirements, the auxiliary stimulation should not raise any safety concerns so long as $\beta \leq 1$. However, from a physiological perspective, a strong cancellation (large β) may in itself cause unwanted sensation. In addition, choosing a large β significantly increases the power consumption, which is highly undesirable in implantable devices. Therefore, SC is added to set the upper limit for allowable canceling-to-stimulating current-ratio to be $\beta_{\max}$, i.e.

$$I_{\mathrm{c},n} \leq \beta_{\max} \cdot I_{\mathrm{s}}, \forall n = 1, 2, \ldots, N \tag{4}$$

In practice, $\beta_{\max}$ needs to be chosen empirically, but for the purpose of this study, $\beta_{\max} = 50\%$ was deemed sufficient (see section 4.1 for additional discussion).

2.2.4. Interference constraint (IC)

Strong cancellation may also interfere with the primary stimulation, potentially leading to the loss of artificial sensation. To constrain this interference on sensation, we first modeled the effect of auxiliary stimulation on cortical excitation underneath the primary stimulating dipole. Specifically, neural excitation generated by external stimulation sources can be quantified by the activating function [25, 26], which is equal to the second spatial derivative of the external potential along the axon of interest. Assuming the stimulation is more likely to activate neurons whose axons are perpendicular to the cortical surface, the activation function af is calculated along the z-direction. This assumption reflects the fact that neurons in cortical gyri are more likely to be activated than those in sulci due to their greater proximity to the cortical surface [27]. Specifically, we calculated af at an observation point (x, y, z) as:

$$af(x, y, z) = \frac{\partial^2 U(x, y, z)}{\partial z^2} \tag{5}$$

where $U(x, y, z)$ denotes the potential at an observation point outside of an axon. Applying $U_{\mathrm{s}}(x, y, z)$ and $U_{\mathrm{c},n}(x, y, z)$ (equations (A1) and (A2)) to the generic

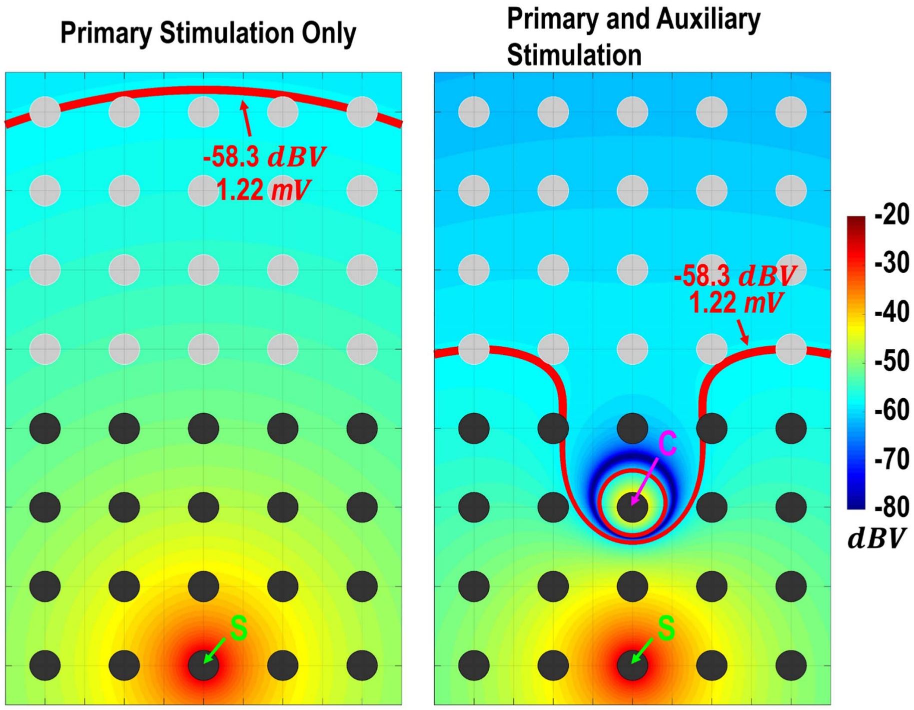

Figure 1. Voltage distributions due to primary stimulation (left) and both primary and auxiliary stimulation (right). Black and grey dots mark the electrodes on stimulating and recording grids, respectively. S - the primary stimulating monopole; C - the canceling (auxiliary) monopole. The voltage distribution due to a monopolar current source (S or C) is described by: $V = I/(4\pi\sigma r)$, where V is the voltage at a distance r from the current source, I is the current amplitude, and σ is the conductivity of the medium [22, 23]. The primary and auxiliary stimulating currents are of opposite polarity, with the auxiliary current set to 25% of the primary current. For a hypothetical analog front-end saturation voltage of 1.22 mV and a bulk conductivity of 1.79 S m^{-1} (cerebrospinal fluid conductivity) [24], the entire recording grid is saturated (left). In contrast, the auxiliary stimulation prevents the saturation entirely without significantly interfering with the primary stimulation (right).

Table 1. Notations for Algorithm 1.

MP	A set of all the model parameters (see appendix C)
A	A set which contains all the possible candidate solutions
$\boldsymbol{os}$	Optimal solution for the optimization problem
$\boldsymbol{cs}$	Candidate solution: containing all the variables to be optimized
$F(\boldsymbol{cs})$	Objective function
PC	Canceling dipole physical constraint ($PC = 1$ for violation; $PC = 0$ otherwise)
SC	Local sensation constraint ($SC = 1$ for violation; $SC = 0$ otherwise)
IC	Interference constraint ($IC = 1$ for violation; $IC = 0$ otherwise)

expression of $af(x,y,z)$, the activating functions due to the primary and auxiliary stimulations at observation points located underneath the primary stimulating dipole are represented by $AF_s(z)$ and $AF_{c,n}(\boldsymbol{cs},z)$, respectively (see appendix E for details).

To quantify the interference due to the auxiliary stimulation, an interference function IF is then defined as the absolute value of the ratio between the activating functions due to the auxiliary and primary stimulations, i.e.

$$IF(\boldsymbol{cs},z) = \left|\frac{\sum_{n=1}^{N} AF_{c,n}(\boldsymbol{cs},z)}{AF_s(z)}\right| \qquad (6)$$

We assume that, at the observation point located underneath the stimulating dipole, if IF is less than the tolerable interference threshold α, the influence of auxiliary stimulation on the artificial sensation can be neglected. In this study, $\alpha = 0.5\%$ is used. However, the exact value of α can only be found empirically (see section 4.1 for additional discussion). This restriction on IF is formulated as the interference constraint (IC), i.e.

$$IF(\boldsymbol{cs},z) \le \alpha, \forall z \in [-6.5, 0] \qquad (7)$$

The average thickness of cerebrospinal fluid (CSF) plus cortex is around 6.5 mm [28, 29]. Therefore, IF is inspected down to 6.5 mm underneath the primary stimulating dipole electrodes. Details can be found in appendix E.

2.2.5. Summary of the optimization framework

Combining the objective function $F(\boldsymbol{cs})$ with the three constraints PC, SC, and IC, the optimization framework is summarized in table 2.

2.3. Validation of the proposed optimization methodology

2.3.1. Phantom tissue

To create a phantom tissue, table salt (Morton Salt, Chicago, IL) was mixed with deionized water, and the mixture was heated until boiling. Food-grade agar

Table 2. Summary of the optimization framework.

Objective		$\boldsymbol{os} = \underset{\boldsymbol{cs}}{\operatorname{argmin}} F(\boldsymbol{cs}), \text{where } F(\boldsymbol{cs}) = \underset{p_{\mathrm{r}}, q_{\mathrm{r}}}{\max} \lvert P_{\mathrm{t}}(\hat{x}_{\mathrm{r}}, \hat{y}_{\mathrm{r}}, \boldsymbol{cs}) \rvert$
Subject to	*PC*	There is no canceling electrode which overlaps with a primary stimulating electrode. There are no canceling dipoles which share electrodes.
	SC	$I_{\mathrm{c},n} \leq \beta_{\max} \cdot I_{\mathrm{s}}, \forall n = 1, 2, \ldots, N$
	IC	$IF(\boldsymbol{cs}, z) \leq \alpha, \forall z \in [-6.5, 0]$ where $IF(\boldsymbol{cs}, z) = \left\lvert \frac{\sum_{n=1}^{N} AF_{\mathrm{c},n}(\boldsymbol{cs}, z)}{AF_{\mathrm{s}}(z)} \right\rvert$

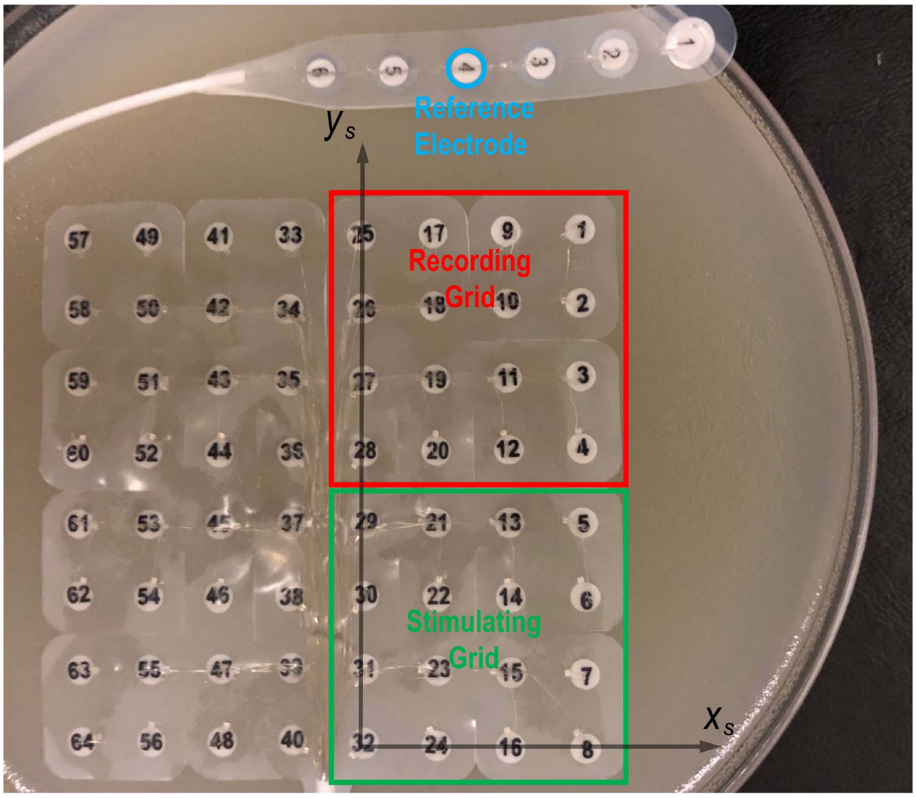

Figure 2. ECoG grids on phantom tissue. The stimulating and canceling dipoles are located on a 4 × 4 stimulating grid. All electrodes on the 4 × 4 recording grid are used to record artifacts. The reference electrode is chosen from the 1 × 6 ECoG strip, positioned far away from the stimulation region. The recording ground is connected to earth ground via the recording amplifier.

(Now Foods, Bloomingdale, IL) was then added into the boiling mixture to prepare a gel compound, which was poured into a Petri dish and an open-ended cylindrical mold. Both were placed in a refrigerator to cool down. The conductivity of the gel was manipulated by table salt concentration [30], and was calculated based on the size and measured resistance of the gel within the cylindrical mold.

2.3.2. Experimental setup

A standard ECoG grid (Ad-Tech, Oak Creek, WI) with platinum electrodes (4 mm diameter, 2.3 mm exposed, 10 mm spacing) delivered stimulating/canceling currents and recorded artifacts, as shown in figure 2. A thin layer of 1× phosphate buffered saline (PBS) (Aldon Corporation, Avon, NY) was added between the grid and the gel to ensure full contact. Due to the limited number of recording amplifiers and the availability of the ECoG grid, two 4×4 arrays of an 8×8 grid were designated as the stimulating and recording grids. In addition, the relative position $(x_{\mathrm{rs}}, y_{\mathrm{rs}})$ and relative angle θ were set to $(0, 40)$ mm and 0 rad. A 1×6 ECoG strip was placed away from the stimulation region and its closest electrode to the central axis of the primary stimulating dipole was designated as the reference.

Figure 3 demonstrates the experimental setup for primary stimulation and recording. The leads of the stimulating dipole were connected to a function generator (supplying an 89 Hz sine wave) in series with an oscilloscope. Since the function generator is a voltage-controlled device, a resistor R_{S} was placed in parallel with the oscilloscope to monitor the stimulating current. The 89-Hz tone was chosen because it produces a narrowband response on the recording grid, which greatly simplifies data analysis. In addition, this frequency is not harmonically related to the 60-Hz noise. An additional function generator and resistor were

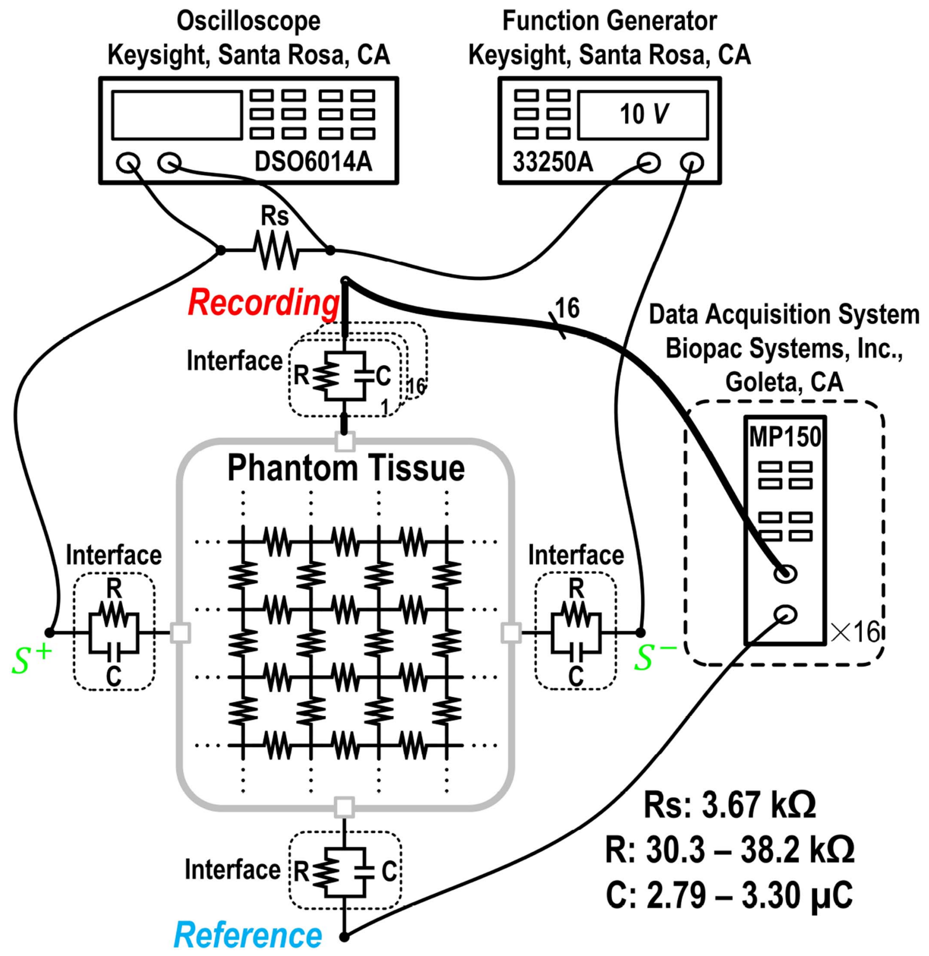

Figure 3. Experimental setup for primary stimulation and recording. S^+ and S^- respectively denote the source and sink electrodes of the stimulating dipole, whose leads were connected to a function generator. The resistor R_S was added to monitor the stimulating current through an oscilloscope. On the recording side, the leads of the 16 recording electrodes were connected to the data acquisition system. All 16 amplifiers shared a common reference voltage.

added for the canceling dipole (details omitted from the figure for clarity). The two function generators were synchronized and produced sine waves with calibrated phase shift in order to create 180° phase difference between stimulating and canceling currents. The leads of the recording grid and the reference electrode were connected to a data acquisition system where the recorded artifacts were amplified by 5,000× and sampled at 4 kHz. We collected 30 s of data under both stimulation-only and stimulation+cancellation conditions, where the strength of cancellation was systematically varied (details below).

2.3.3. Estimation of stimulating current I_s

For simplicity, a fixed value of the stimulating current, I_s, was used across all experiments. To account for impedance differences across stimulation sites and find I_s that works for all experiments, the following analysis was used. According to figure 3, the total impedance seen by the function generator consists of the impedance of the electrode-electrolyte interfaces, resistance of the current monitoring resistor, R_S, and the equivalent resistance of the phantom tissue connected in series. To estimate this impedance, electrode-electrolyte interfaces were modeled as parallel RC circuits [31], and the phantom tissue was modeled as a distributed resistive network (figure 3). The total impedance of the interfaces and phantom tissue was then measured across frequency. Subsequently, curve-fitting was applied to the impedance frequency response to estimate the resistance and capacitance of these interface models as well as the equivalent resistance of the phantom tissue. Based on these estimated values, the total impedance of the interfaces and phantom tissue was calculated to be 562–1928 Ω at 89 Hz. The result is consistent with clinical measurement [32, 33]. Therefore, the total impedance seen by the function generator was calculated to be 4–6 kΩ. Given that the maximum voltage of the function generator was 10 V, this total impedance allowed an I_s of 1.5 mA across all the cases.

2.3.4. Experiments

The experimental setup (discussed in section 2.3.2) was used in four different cases, shown in figure 4, to demonstrate the performance of the optimization algorithm under different stimulating dipoles. The phantom tissue with a conductivity of 1.79 S m^{-1} was

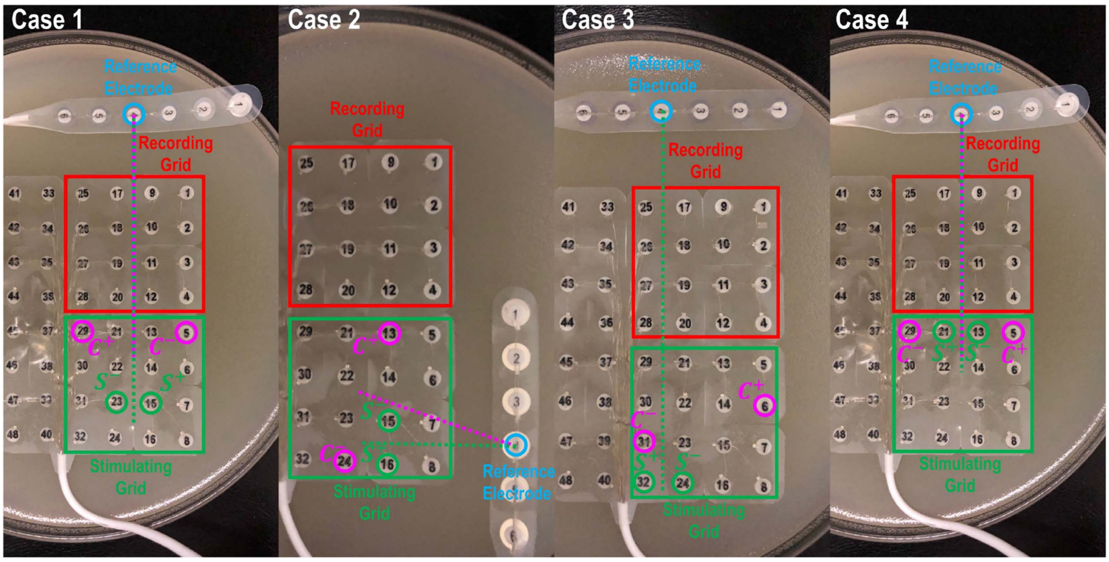

Figure 4. Physical configuration of experiments for all the cases. Case 1: electrode pair 15-23 (source-sink) realized the primary stimulating dipole. Electrode pairs 22-14, 21-13, 30-6, and 29-5 (shown) were used one at a time as the canceling dipole. Reference electrode was placed far away from the stimulating grid near the hypothetical zero-potential line at the central axis of both stimulating and canceling dipoles. Case 2: electrode pair 16-15 realized the primary stimulating dipole. Electrode pairs 13-8, 21-8, 13-24 (shown), and 5-24 were used one at a time as the canceling dipole. When possible, the reference electrode was placed near the central axes of both the stimulating and canceling dipoles (shown). Otherwise, it was placed near the central axis of the stimulating dipole. Case 3: electrode pair 32-24 realized the primary stimulating dipole. Electrode pairs 6-31 (shown), 7-30, 6-30, and 7-31 were used one at a time as the canceling dipole. Reference electrode was placed far away from and near the central axis of the primary stimulating dipole. Case 4: electrode pair 21-13 realized the primary stimulating dipole and electrode pair 5-29 was used as the canceling dipole. Reference electrode was placed far away from the stimulating grid near the central axes of both stimulating and canceling dipoles.

chosen to mimic the bulk conductivity of subdural head tissues which is dominated by the CSF [24]. The dipole model used to describe the artifact propagation (see appendix A) requires an assumption of an infinitely far reference. Since this is not physically achievable in reality, the reference is placed far from the primary stimulating dipole on the zero potential line to best fulfill the referencing assumption.

A single electrode pair was used as the stimulating dipole. Case 1 is the most straightforward situation in which the stimulating dipole is oriented horizontally and its central axis coincides with the axis of symmetry of the recording grid. Case 2 is similar except that the stimulating dipole was oriented vertically. In Case 3, the stimulating dipole is oriented horizontally, while the recording grid is not symmetric with respect to the dipole's central axis. Case 4 mimics the worst-case scenario, where the horizontally oriented stimulating dipole is adjacent to the recording grid, so the artifacts will be projected the furthest into the recording grid.

Table 3. Model parameters for Cases 1–4.

Geometric characterization parameters	X_s, Y_s	4, 4
	X_r, Y_r	4, 4
	d	10 mm
	x_{rs}, y_{rs}	0 mm, 40 mm
	θ	0 rad
Dipole model parameter	σ	1.79 S/m
Primary stimulation model parameters	x_s^+, y_s^+	20 mm, 10 mm (Case 1) 20 mm, 0 mm (Case 2) 0 mm, 0 mm (Case 3) 10 mm, 30 mm (Case 4)
	x_s^-, y_s^-	10 mm, 10 mm (Case 1) 20 mm, 10 mm (Case 2) 10 mm, 0 mm (Case 3) 20 mm, 30 mm (Case 4)
	I_s	1.5 mA
Number of canceling dipoles	N	1
Constraint system parameters	$\beta_{\max}$	50%
	α	0.5%

2.3.5. Running optimization algorithm

Before running the optimization algorithm, the model parameters, as listed in table C1, need to be specified. To this end, the geometric characterization and primary stimulation parameters were extracted for each case based on figure 4. As discussed in section 2.2.3 and 2.2.4, we chose $\beta_{\max} = 50\%$ and $\alpha = 0.5\%$, and we assumed a single canceling dipole ($N = 1$). As listed in table 3, all the cases shared the same model parameters except for the primary stimulation locations. Based on these parameters, the optimization algorithm was executed for each case and the optimal canceling patterns were found. These optimal patterns were verified by simulation (details in section 2.3.6) and experimentally (details in section 2.3.7), respectively.

2.3.6. Simulation verification

To illustrate the effectiveness of the optimal canceling pattern in each case, the voltage distributions were calculated using equations (A3)–(A5) for the following conditions: (i) stimulating dipole only, and (ii) both stimulating and the optimal canceling dipoles. These voltage values were color-coded and mapped onto the grid for comparison. In addition, to characterize the effectiveness of the optimal canceling pattern, the artifact suppression was quantified by dividing the largest artifact magnitude under conditions (i) and (ii).

To further verify the effectiveness of the optimal canceling pattern, the location and/or the canceling ratio, β, of the optimal canceling dipole were perturbed. The corresponding artifact suppression was then quantified and compared to that of the optimal solution. For example, in Case 1, in addition to the optimal canceling dipole (electrode pair: 30–6), the following canceling dipole locations were tested: 22–14, 21–13, and 29–5. Note that these are the immediate neighbors of the optimal pair 30–6 (see figure 4). For all the canceling dipoles, β was swept from 0 to $\beta_{\max}$ in 1% increments. Similar analysis was applied to other cases. The only exception was Case 4, where it was obvious that the perturbation of the optimal canceling dipole location would not produce competitive results.

2.3.7. Experimental verification

The above simulation verification and analysis were then replicated experimentally using the procedure discussed in section 2.3.2. The 30 s of data recorded under both stimulation only and stimulation+cancellation conditions were analyzed offline using Matlab. The data were first filtered by a bandpass finite impulse response (FIR) filter with 85–93 Hz passband (for an 89 Hz test input), 0.1% inband ripple, and 40 dB stopband attenuation. Each set of the filtered data was decomposed into 30 non-overlapping segments. These segments were then converted into frequency domain, and their amplitude spectra were calculated and averaged to reduce noise. For all the recording channels, the artifacts' amplitudes were estimated as the values of the voltage spectra at 89 Hz. These values were then spatially interpolated, color-coded, and mapped for analysis. Similar to section 2.3.6, the optimal canceling pattern (as found by the algorithm) was experimentally tested and compared to those found by perturbation.

3. Results

3.1. Simulation results

Figures 5(A) and (B) respectively show the spatial distribution of simulated artifacts before and after optimal cancellation for Case 1. The optimal canceling pattern was a dipole located at the electrode pair 30-6 with $\beta = 18\%$. We found these parameters by running the optimization algorithm as explained in section 2.3.5. Table 4 shows the algorithm run time for this as well as other cases. Note that the symmetric arrangement of the stimulating and canceling dipoles caused the symmetry in the spatial distribution of artifacts. By applying optimal cancellation, the largest artifact experienced by the recording grid decreased from -71.7 dBV to -100.4 dBV for a total artifact suppression of 28.7 dB.

Figures 5(C) and (D) show the equivalent maps for Case 2. The optimal canceling pattern reduced the largest artifact by 11.7 dB. This result is inferior to Case 1 due to the unfavorable (vertical) orientation of the stimulating dipole.

Figures 5(E) and (F) show the spatial distribution of simulated artifacts for Case 3. An optimal suppression of 16.0 dB was achieved, but the pre-cancellation artifacts were smaller than those in Case 1 and 2. It is worth mentioning that the artifact tends to be larger at electrodes located away from the central axis of the stimulating dipole. Hence, as shown in figure 5(F), the source electrode of the canceling dipole, obtained from the optimization algorithm, was placed closer to the recording grid than the sink to provide larger cancellation to the recording sites further away from the central axis.

Figures 5(G) and (H) show the equivalent distribution for Case 4. Intuitively, higher artifact suppression can be achieved by continuously increasing β. However, increasing β beyong 25% cause violation of *IC* (refer to section 2.2.4). Therefore, $\beta = 25\%$ was chosen by the optimization algorithm as the optimal solution, resulting in an artifact suppression of 2.2 dB.

Perturbations of the optimal canceling dipole location and β were then simulated and compared to the optimal solution for each case (see figure 6). For Cases 1–3, three additional competitive canceling dipole locations were tested (see section 2.3.6). In addition, since the optimal β never exceeded 20%, the perturbations of β up to 20% were selected to show in figure 6. For Case 4, the upper bound for β was 25% (as discussed above), and no competitive canceling dipoles could be created by location perturbation (as discussed in section 2.3.6). In figure 6, it is clearly seen that the optimal solutions demonstrate the largest amount of artifact suppression. These optimal solutions for Cases 1–4 are summarized in table 5.

3.2. Experimental results

Following validation of the optimization framework with simulation, phantom tissue experiments (see section 2.3.7) were conducted to further demonstrate the effectiveness of the proposed algorithm. Similar to figure 5, the artifact spatial distributions were visualized with and without the optimal canceling pattern (see figure 7). A more detailed collection of artifact suppression maps can be found in the supplementary material (stacks.iop.org/JNE/17/026038/mmedia).

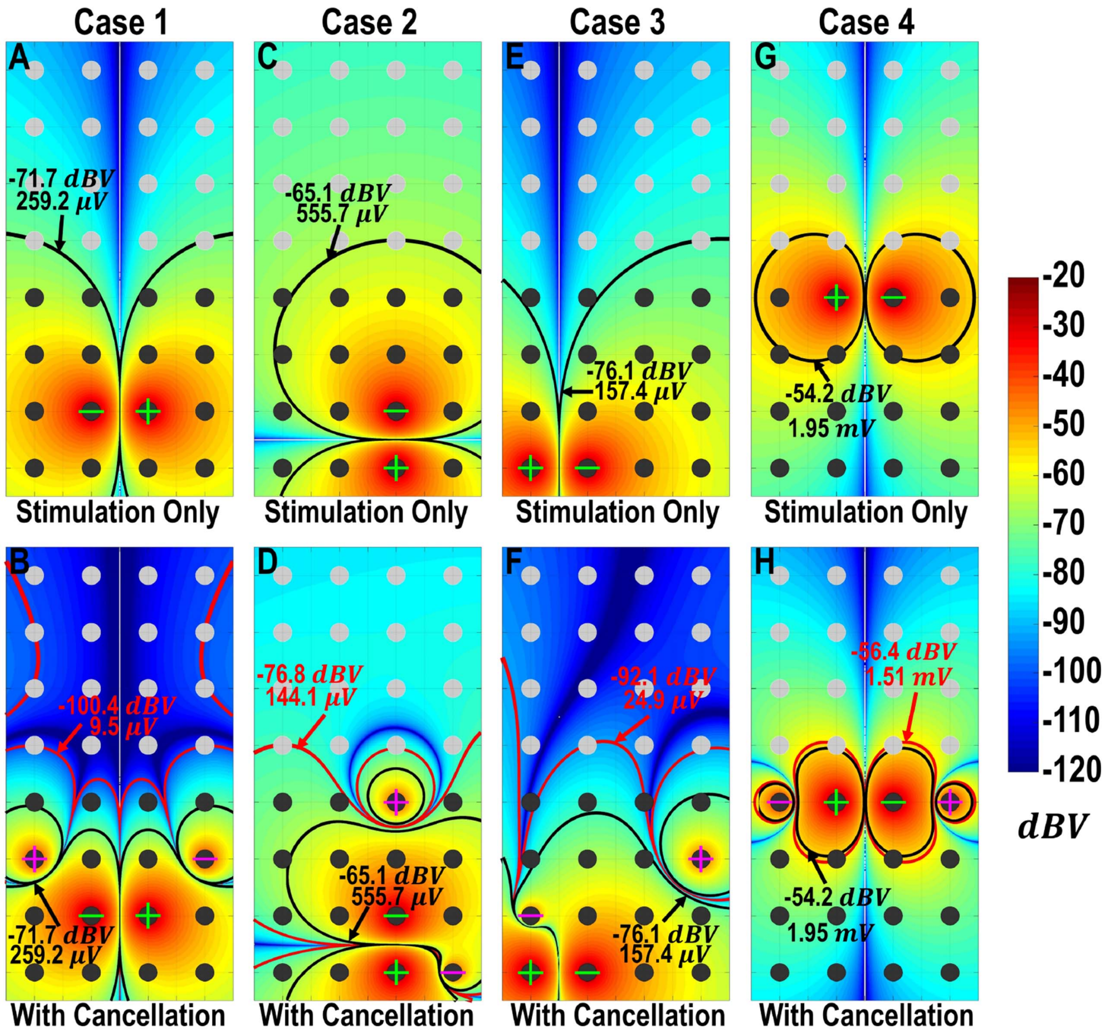

Figure 5. Spatial distribution of simulated artifacts under stimulation only and stimulation + optimal cancellation conditions for Cases 1–4. Grey: recording grid. Black: stimulating grid. Green: stimulating dipole. Magenta: canceling dipole. A: Case 1–the stimulating dipole is formed by electrode pair 15–23 (see figure 4 for reference). Black contour marks the largest observed artifact. B: Case 1–the optimal canceling pattern is formed by using electrode pair 30–6 with $\beta = 18\%$. The largest-artifact contour (red) indicates the artifact has been suppressed from 259.2 to 9.5 μV (or by 28.7 dB). At the same time, the original largest-artifact contour (black) is well outside the recording grid. C: Equivalent of A for Case 2. D: Equivalent of B for Case 2 (optimal $\beta = 13\%$). An artifact suppression of 11.7 dB has been achieved. E: Equivalent of A for Case 3. F: Equivalent of B for Case 3 (optimal $\beta = 10\%$). An artifact suppression of 16.0 dB has been achieved. G: Equivalent of A for Case 4. H: Equivalent of B for Case 4 (optimal $\beta = 25\%$). An artifact suppression of 2.2 dB has been achieved.

Table 4. Algorithm run times (Intel$^{®}$ Core^{TM} i5-7400, 8 GB RAM).

Case 1	13.367 sec
Case 2	14.692 sec
Case 3	13.566 sec
Case 4	13.514 sec

The optimal solutions tested experimentally are summarized in table 5. The comparison between experimental and simulation results indicates that the optimization algorithm makes accurate predictions about the artifact suppression.

Similar to figure 6, perturbations of the optimal canceling dipole location and β were experimentally tested (see figure 8). A comparison with the plots of figure 6 reveals that experimental results closely follow those obtained by simulations. More precisely, in Case 1, the best artifact suppression was reported by both the experiment and simulation when the electrode pair 30-6 with $\beta = 18\%$ was used as the canceling pattern. Moreover, referring to figure 8, the artifact suppression first increases with β for canceling dipoles 30-6, 21-13, and 29-5, before it reaches its peak value. The reason for this monotonically increasing trend is that the artifact due to cancellation is still smaller than that due to the primary stimulation. For larger β values, the artifact suppression decreases (even becomes negative) as the artifact due to cancellation starts to dominate. For canceling dipole 22-14, even with a β of 20%, the artifact due to primary stimulation still dominates and artifact suppression shows a monotonic behavior. This is because the electrode pair 22-14 is in the vicinity of the primary stimulation, which requires larger β to achieve the same amount of

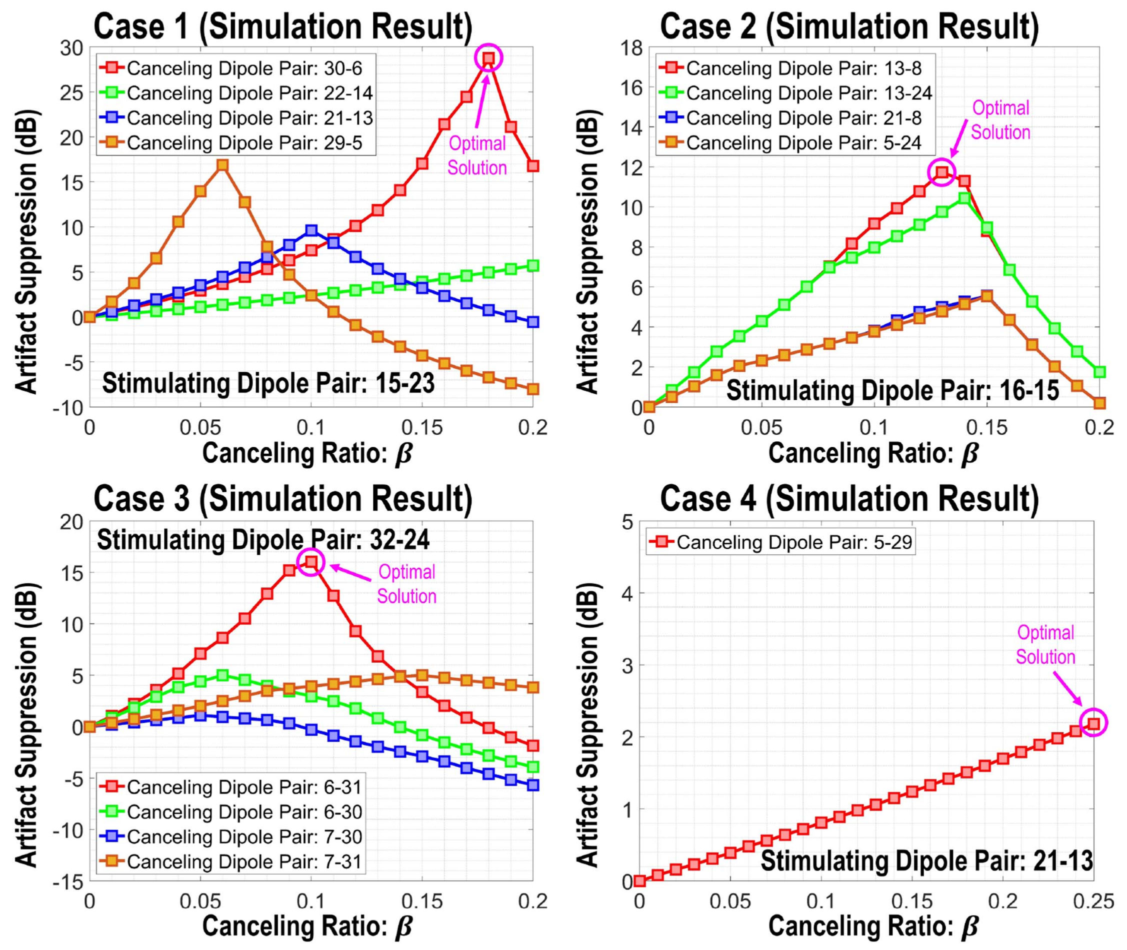

Figure 6. Perturbation analysis: simulation results. In Case 1, the perturbations of canceling dipole location and β demonstrate inferior artifact suppression compared to the optimal solution (marked in magenta) found by the optimization algorithm. Similarly, Case 2 and Case 3 exhibit superiority of the optimal solutions. In Case 4, the artifact suppression increases monotonically with β as predicted. The largest artifact suppression happens when β reaches 25% (limited by IC). This result is consistent with the optimal solution found by the optimization algorithm.

Table 5. Algorithmically optimal solutions tested in simulation and experimentally.

	Case 1		Case 2		Case 3		Case 4	
Result type	Sim	Exp	Sim	Exp	Sim	Exp	Sim	Exp
Largest artifact among all the recording sites without cancellation (μV)	259.2	350.5	555.7	767.2	157.4	151.2	1 950.2	2 693.1
Largest artifact among all the recording sites with optimal cancellation (μV)	9.5	25.1	144.1	204.4	24.9	31.6	1 510.0	1 995.2
Artifact suppression (dB)	28.7	22.9	11.7	11.5	16.0	13.6	2.2	2.6
Optimal canceling dipole (source-sink)	30–6	30–6	13–8	13–8	6–31	6–31	5–29	5–29
Optimal canceling ratio β_{opt}	18%	18%	13%	13%	10%	10%	25%	25%

artifact suppression as the other canceling dipoles in this case.

For Case 2, the optimal solution for the simulation and experiment were similar except for a 1% difference in β. Additionally, the artifact suppression plots for the electrode pairs 13-24 and 13-8 closely follow one another with the latter providing slightly better cancellation. This slight improvement was also captured by the simulation, as shown in figure 6, which further proves the necessity of this algorithm for cases where visual inspection alone is incapable of finding the optimal solutions.

For Case 3, the optimal solution found by the algorithm was confirmed experimentally. In Case 4, the optimal solution also matches the one found experimentally. In addition, the artifact suppression increases monotonically, as also observed in figure 6. The reason for keeping $\beta \leq 25\%$ is that, beyond

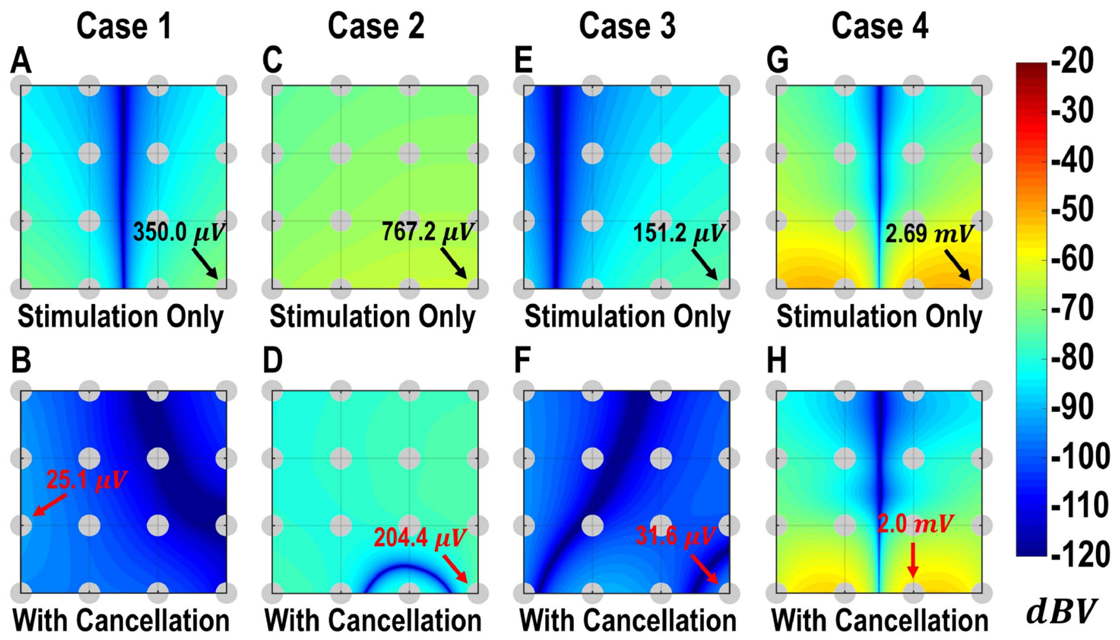

Figure 7. Artifact spatial distribution under stimulation only and stimulation+optimal cancellation conditions for Cases 1–4. Grey: recording grid. Unlike figure 5, the artifact distribution outside the recording grid is not shown because artifacts were only recorded within the recording grid. (see section 2.3.7). A: Case 1–the stimulating dipole is formed by electrode pair 15-23 (see figure 4 for reference). The largest artifact was recorded as 350.5 μV (marked in black). B: Case 1–the optimal canceling pattern is formed by using electrode pair 30–6 with $\beta = 18\%$. The largest artifact after the optimal cancellation was measured as 25.1 μV (marked in red), leading to an artifact suppression of 22.9 dB. C: Equivalent of A for Case 2. The largest artifact was recorded as 767.2 μV. D: Equivalent of B for Case 2 (canceling pair 13–8 with $\beta = 13\%$, leading to 11.5 dB artifact suppression). E: Equivalent of A for Case 3. The largest artifact was recorded as 151.2 μV. F: Equivalent of B for Case 3 (canceling pair 6–13 with $\beta = 10\%$, leading to 13.6 dB artifact suppression). G: Equivalent of A for Case 4. The largest artifact was recorded as 2693 μV. H: Equivalent of B for Case 4 (canceling pair 5–29 with $\beta = 25\%$, leading to 2.6 dB artifact suppression).

this point, the optimization algorithm found *IC* to be violated (*IF* exceeds α). Note that calculating *IF* requires a full 3D voltage distribution, which is achievable in simulations but not experimentally. Therefore, in our experiments, we chose the same range of β values as in simulations.

In summary, the experimentally optimal canceling patterns closely follow the optimal one found by the proposed optimization algorithm. Additionally, comparing figure 6 with figure 8 verifies that the results from phantom tissue experiments match those from simulations.

4. Discussion

In this work, we have developed an optimization framework based on the electric dipole model to optimally suppress stimulation artifacts across ECoG recording electrodes. Our simulation and experimental results confirmed that the optimal canceling patterns found by the algorithm provided superior artifact suppression compared to other solutions. Additionally, the optimal canceling dipole found by the algorithm performed consistently in both simulations and experiments (there was only a minor disagreement in Case 2, where β was off by 1%). Generally, experimentally measured artifacts were stronger than the simulated ones (see table 5). This discrepancy could be explained by the model assuming an unbounded, isotropic, and homogeneous volume conduction. In contrast, for the phantom tissue placed in a Petri dish, this assumption generally does not hold. Its finite volume and non-negligible boundary conditions may have resulted in a stronger electric field than the dipole model's prediction. Additionally, the model assumed infinitely far reference, whereas in experiments, the reference electrode was typically 3 cm to 9 cm away. Infinitely far reference could be mimicked experimentally by placing the reference electrode at the intersection of the stimulating and canceling dipole axes (e.g. figure 4: Case 1). However, this was not always possible (e.g. figure 4: Case 3). Nevertheless, these discrepancies did not seem to affect the solution, i.e. the optimal canceling patterns were nearly identical in simulations and experiments.

An important feature of our technique is that it suppresses artifacts before they reach recording electrodes. This feature is especially useful for future fully implantable BD-BCIs, which will require ULP operation and will, therefore, be highly susceptible to amplifier saturation. In contrast, existing artifact mitigation techniques, whether focused on analog front-ends [11, 12] or digital filtering [11, 13, 14], require that the recorded signals remain in the linear region (without saturation). For example, [11] used adaptive filters to estimate the artifact contribution to recorded signals, followed by the subtraction of

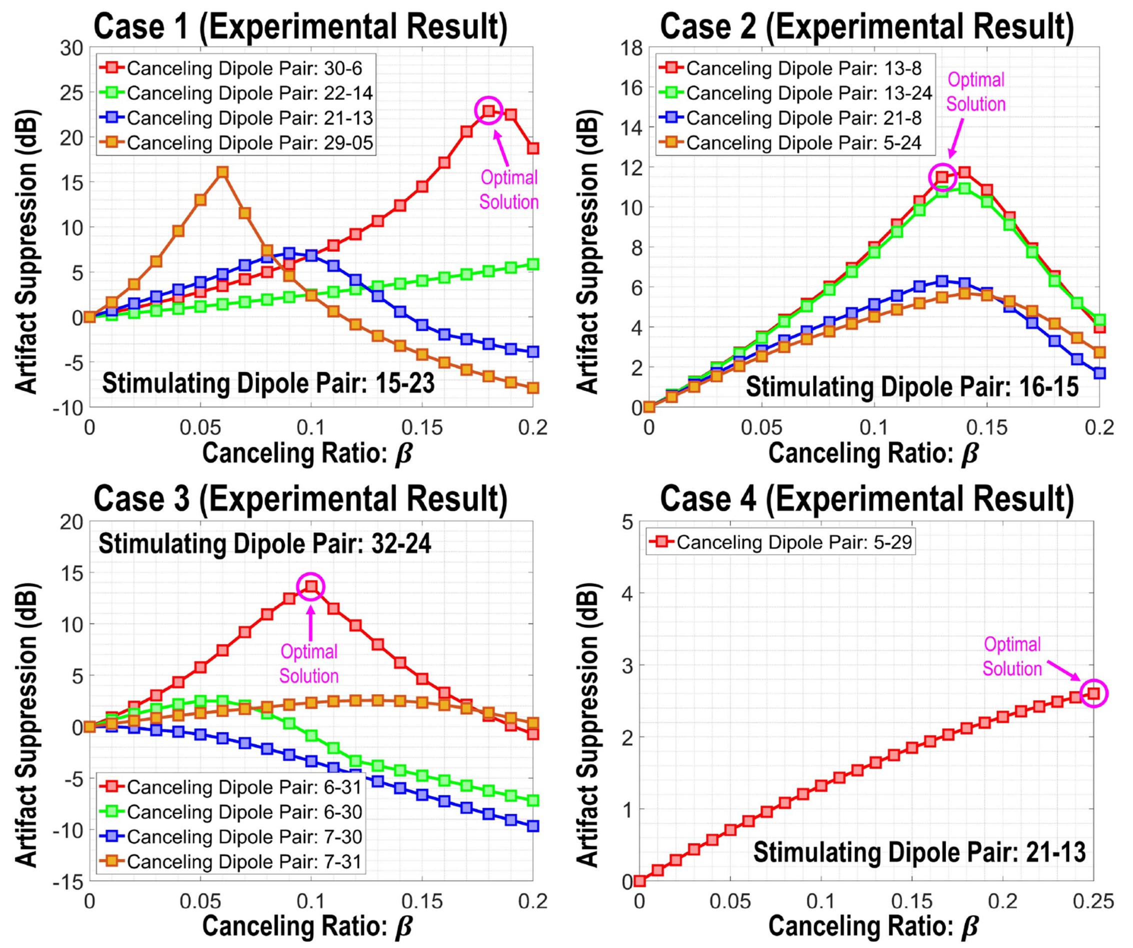

Figure 8. Perturbation analysis: experimental results. In Case 1, the perturbations of canceling dipole location and β demonstrate inferior artifact suppression compared to the optimal solution (marked in magenta) found by the optimization algorithm. In Case 2, instead of the optimal solution (electrode pair 13-8 with $\beta = 13\%$), the same canceling dipole with $\beta = 14\%$ demonstrates the largest artifact suppression. Similarly to Case 1, Case 3 exhibits superiority of the optimal solutions. In Case 4, the artifact suppression increases monotonically with β as predicted. The largest artifact suppression happens when β reaches 25% (limited by *IC*). This result is consistent with the optimal solution found by the optimization algorithm.

these artifact components before amplification at the front-end. Although capable of achieving large artifact suppression (42 dB), this technique is not applicable if the front-end is saturated. The technique in [34] proposed artifact cancellation by exploiting symmetrical differential stimulation. However, this technique places constraints on the spatial arrangement of stimulation and recording channels. In contrast, our approach was validated using four different cases, underscoring the applicability of our method under a variety of spatial arrangements. Finally, we note that our method can be used in conjunction with these existing artifact mitigation techniques, which can lead to further suppression of stimulation artifacts.

In conclusion, the simulation and experimental results suggest that our artifact cancellation approach, along with the optimization framework, could be used in future fully-implantable BD-BCI systems to significantly suppress stimulation artifacts or protect its ULP front-end from saturation.

4.1. Constraint Parameters $\beta_{\max}$ and α

In clinical practice, I_s is typically chosen as the minimum current exceeding the sensation threshold. Thus, theoretically, any $\beta < 100\%$ should not cause unwanted sensation (see section 2.2.3). Since brain tissue excitability is location dependent [5], we limited the amplitude of the auxiliary stimulation by setting $\beta_{\max} = 50\%$. Our algorithm yielded the optimal values of β ranging from 10% to 25% (See figures 6 and 8), suggesting that $\beta_{\max}$ was chosen appropriately. From an optimization standpoint, this means that the constraint *SC* was not active. For practical applications, $\beta_{\max}$ must be determined empirically, although the values obtained in this study may serve as an informed initial guess.

To reduce the interference of auxiliary stimulation with the primary stimulation (see section 2.2.4), we chose $\alpha = 0.5\%$ as an arbitrary small number. However, in practical applications, α must be chosen empirically. If this value is not sufficiently small, then the primary stimulation dipole may be weakened by the auxiliary dipole to the point of no longer eliciting sensation. A potential mitigation strategy then would be to increase the primary stimulating current, I_s, above the sensation threshold to compensate for this interference. Note that the upper bound on I_s is determined by the FDA charge density guidelines. For example, since the sensation can be elicited with as low as 12.7 μC cm^{-2} phase^{-1} [5], which is lower than the FDA recommended safety limit of 25 μC cm^{-2} phase^{-1} [35], the above strategy of countering interference by increasing I_s seems feasible.

4.2. Multi-polar Cancellation

In this study, a single canceling dipole ($N = 1$) was used. This limitation was imposed by the complexity of the experimental setup and the need to synchronize two independent function generators (Introducing additionally canceling dipole would require yet another function generator to be added). However, the simulation results (figures omitted in the interest of space) indicate that $N = 2$ provides a superior solution. For example in Case 1, the artifact suppression went from 28.7 dB ($N = 1$) to 39.5 dB ($N = 2$). Although multi-dipolar cancellation ($N > 1$) can boost the artifact suppression, it will also increase computational cost because the run time of the algorithm increases exponentially with N. Additionally, it leads to an increase in power consumption which is highly undesirable in fully-implantable devices. This trade-off between power consumption and artifact cancellation suggests that N needs to be chosen empirically in practice to prevent the front-end amplifiers from reaching saturation. Our future plans involve designing a multi-polar stimulator that will seamlessly integrate all the features of this optimization algorithm. In addition, human tests will be conducted. However, these tests require FDA clearance and thus could not be performed at this point.

4.3. Limitations

4.3.1. Limitation due to grid geometry

Our approach is primarily limited by the number of electrodes available for cancellation. Take for example Case 4, where the primary dipole lies adjacent to the recording electrodes. However, the addition of auxiliary stimulation may still suppress artifacts (cf table 5), which could mean the difference between saturation and non-saturation. Ultimately, our approach may not always succeed in cases like this. However, these extremely unfavorable primary dipole configurations are not very likely to occur. These considerations also suggest that our technique would favor higher-density ECoG grids [36], as there is a larger solution space to search over.

4.3.2. Single tone verification

We chose a single 89-Hz tone as our test signal rather than a broadband biphasic square pulse train to simplify data analysis (see section 2.3.2). Compared to a single tone, the group delay varies across frequency for broadband signals. However, we previously showed that the peaks of stimulation artifacts are tightly phase-locked across spatially distributed ECoG electrodes [20, 21], suggesting that the capacitive effects can be neglected. Therefore, the results from this study are expected to generalize to more realistic broadband stimulation signals.

4.3.3. Computational efficiency

The execution times (table 4) show that the algorithm can produce solutions within seconds for a relatively small (4 × 4) grid. Generally, the complexity of the algorithm scales quadratically with the number of electrodes ($\mathcal{O}(n^2)$), which given a typical grid size of 32 electrodes, is not expected to cause any computational concerns. The problem becomes exponentially more complex with multi-dipolar ($N > 1$) cancellations. For example, for $N = 2$ the run times were 5–10 min. For larger grids, this could become prohibitively expensive and these computations could be accelerated by finding β through a gradient descent approach. Note, however, that unlike the search method employed here, such an approach may return a locally optimal solution.

4.3.4. Curvature of the ECoG grid

We assumed that the recording and stimulating grids lie on a planar surface (A), which is justified for sensory and motor cortices—the primary areas of interest in BD-BCI applications. Consequently, our simulations and experimental set up were designed to reflect this situation. Note, however, that the dipole model and the interference constraint are natively 3D, and so our approach could be extended to cortical surfaces with prominent curvature. The experimental validation of such a scenario would, however, be challenging and was not pursued in this study.

5. Conclusion

This work presents a novel technique for the suppression of artifacts due to cortical electrostimulation. The method introduces auxiliary (canceling) dipoles and proceeds to find the parameters of these dipoles through a constrained optimization framework. These optimal canceling patterns significantly reduce the stimulation artifacts before they reach the recording grid and analog front-ends, which can potentially prevent amplifiers from saturation. Our method is especially useful in future fully-implantable BCI systems which are required to operate in an ULP regime and are therefore highly susceptible to saturation. In addition, our method is compatible with existing techniques which could collectively result in an even greater degree of artifact suppression. Our future plans involve the development of a custom ULP cortical stimulator that can seamlessly integrate multi-polar features and the synchronization of primary and auxiliary dipoles. We will also test the function of such a stimulator in humans.

6. Conflicts of interest

The authors declare no competing financial interests.

Acknowledgment

This work was supported by the National Science Foundation (Award Number: 1646275).

A. Dipole Model

According to the dipole model, the spatial voltage distribution due to subdurally delivered stimulation can be expressed as [15]:

$$U_{\mathrm{s}}(x,y,z) = \frac{I_{\mathrm{s}}}{4\pi\sigma}\left[\frac{1}{r_{\mathrm{s}}^{+}(x,y,z)} - \frac{1}{r_{\mathrm{s}}^{-}(x,y,z)}\right] \tag{A1}$$

where $U_{\mathrm{s}}(x,y,z)$ is the voltage amplitude seen at the observation point (x,y,z), I_{s} is the current amplitude of the primary stimulation, σ is the average bulk conductivity of the brain tissue and tissues between the electrodes and the brain (arachnoid, cerebrospinal fluid, blood vessels, and pia mater). These layers are assumed to be isotropic, homogeneous, and purely resistive volume conductors [23, 25]. r_{s}^{+} and r_{s}^{-} denote the Euclidean distances between the point (x,y,z) and the stimulating dipole source and sink electrodes, respectively. Note that the voltage and current are represented in amplitude since stimulation patterns are typically chosen as constant-magnitude biphasic pulse trains. Similar to equation (A1), the spatial voltage distribution due to the n^{th} auxiliary stimulation can be expressed as:

$$U_{\mathrm{c},n}(x,y,z) = -\frac{I_{\mathrm{c},n}}{4\pi\sigma}\left[\frac{1}{r_{\mathrm{c},n}^{+}(x,y,z)} - \frac{1}{r_{\mathrm{c},n}^{-}(x,y,z)}\right] \tag{A2}$$

where $n = 1, \ldots, N$ (N–the total number of canceling dipoles), $I_{\mathrm{c},n} = \beta_n \cdot I_{\mathrm{s}}$ is the current amplitude of the n^{th} auxiliary stimulation ($\beta_n \in [0,1]$), and $r_{\mathrm{c},n}^{+}$ and $r_{\mathrm{c},n}^{-}$ denote the Euclidean distances between the point (x,y,z) and the source and sink electrodes of the nth canceling dipole, respectively.

Due to the proximity and relatively small sizes of the arm or leg primary motor/sensory cortices, which are the main target areas for BD-BCIs, we assume that the curvature of ECoG grids can be neglected, even for those grids placed over the cortical convexity. Thus, a two-dimensional dipole model is sufficient to describe the voltage distribution at the cortical surface:

$$V_{\mathrm{s}}(x,y) = U_{\mathrm{s}}(x,y,z)|_{z=0} \tag{A3}$$

$$V_{\mathrm{c},n}(x,y) = U_{\mathrm{c},n}(x,y,z)|_{z=0} \tag{A4}$$

where $z = 0$ is the plane of the ECoG grid. The net voltage amplitude V_{t} is obtained as the algebraic summation of stimulating and canceling voltage amplitudes, i.e.

$$V_{\mathrm{t}}(x,y) = V_{\mathrm{s}}(x,y) + \sum_{n=1}^{N} V_{\mathrm{c},n}(x,y) \tag{A5}$$

B. Definitions of a candidate solution *cs* and the optimal solution *os*

Since a canceling pattern involves all the canceling dipole locations and canceling currents, a candidate solution ***cs*** can be defined as:

$$\boldsymbol{cs} = \{I_{\mathrm{c},1}, x_{\mathrm{c},1}^{+}, y_{\mathrm{c},1}^{+}, x_{\mathrm{c},1}^{-}, y_{\mathrm{c},1}^{-}, I_{\mathrm{c},2}, x_{\mathrm{c},2}^{+}, y_{\mathrm{c},2}^{+}, x_{\mathrm{c},2}^{-}, y_{\mathrm{c},2}^{-}, \ldots, I_{\mathrm{c},N}, x_{\mathrm{c},N}^{+}, y_{\mathrm{c},N}^{+}, x_{\mathrm{c},N}^{-}, y_{\mathrm{c},N}^{-}\} \tag{B1}$$

where $(x_{\mathrm{c},n}^{+}, y_{\mathrm{c},n}^{+})$ and $(x_{\mathrm{c},n}^{-}, y_{\mathrm{c},n}^{-})$ are the coordinates of the source and sink electrodes of n^{th} canceling dipole ($n = 1, 2, \ldots, N$ and N is the total number of auxiliary stimulating dipoles used for cancellation, see appendix C), and $I_{\mathrm{c},n} = \beta_n \cdot I_{\mathrm{s}}$ is the amplitude of the current delivered by the n^{th} canceling dipole. Accordingly, the optimal solution ***os*** is defined as:

$$\boldsymbol{os} = \{I_{\mathrm{c},1}^{\mathrm{opt}}, x_{\mathrm{c},1}^{+,\mathrm{opt}}, y_{\mathrm{c},1}^{+,\mathrm{opt}}, x_{\mathrm{c},1}^{-,\mathrm{opt}}, y_{\mathrm{c},1}^{-,\mathrm{opt}}, I_{\mathrm{c},2}^{\mathrm{opt}}, x_{\mathrm{c},2}^{+,\mathrm{opt}}, y_{\mathrm{c},2}^{+,\mathrm{opt}}, x_{\mathrm{c},2}^{-,\mathrm{opt}}, y_{\mathrm{c},2}^{-,\mathrm{opt}}, \ldots, I_{\mathrm{c},N}^{\mathrm{opt}}, x_{\mathrm{c},N}^{+,\mathrm{opt}}, y_{\mathrm{c},N_{\mathrm{opt}}}^{+,\mathrm{opt}}, x_{\mathrm{c},N}^{-,\mathrm{opt}}, y_{\mathrm{c},N}^{-,\mathrm{opt}}\} \tag{B2}$$

where $\left(x_{\mathrm{c},n}^{+,\mathrm{opt}}, y_{\mathrm{c},n}^{+,\mathrm{opt}}\right)$ and $\left(x_{\mathrm{c},n}^{-,\mathrm{opt}}, y_{\mathrm{c},n}^{-,\mathrm{opt}}\right)$ represent the optimal locations of the source and sink electrodes of n^{th} canceling dipole, and $I_{\mathrm{c},n}^{\mathrm{opt}}$ is the optimal amplitude of the current delivered by the nth canceling dipole ($n = 1, 2, \ldots, N$).

C. Mathematical model

To construct the mathematical model characterizing concurrent ECoG stimulation and recording, a set of model parameters *MP*, listed in table C1, is introduced. Details are discussed in the following sections.

We define electrodes contact spacing in both stimulating and recording grids to be d, and the number of rows and columns of stimulating grid to be Y_{s} and X_{s}, respectively, as shown in figure C1(A). Thus, a stimulation electrode location S is represented as:

$$(x_{\mathrm{s}}, y_{\mathrm{s}}) = (p_{\mathrm{s}} \cdot d, q_{\mathrm{s}} \cdot d), \quad p_{\mathrm{s}} = 0, 1, \ldots, X_{\mathrm{s}} - 1, \quad q_{\mathrm{s}} = 0, 1, \ldots, Y_{\mathrm{s}} - 1 \tag{C1}$$

Since both primary and auxiliary stimulating dipoles deliver currents through the same stimulating grid, we also define a canceling electrode location

Table C1. Mathematical model parameters (unitless unless noted otherwise).

Geometric characterization parameters	X_s, Y_s	Number of columns and rows of the stimulating ECoG grid
	X_r, Y_r	Number of columns and rows of the recording ECoG grid
	d (mm)	Electrodes contact spacing
	x_{rs}, y_{rs} (mm)	Relative position
	θ (rad)	Relative angle
Dipole model parameter	σ (S/m)	Conductivity
Primary stimulation model parameters	x_s^+, y_s^+ (mm)	Stimulating dipole source electrode location
	x_s^-, y_s^- (mm)	Stimulating dipole sink electrode location
	I_s (mA)	Stimulating current
Number of canceling dipoles	N	Number of auxiliary dipoles used to suppress artifacts
Constraint system parameters	$\beta_{\max}$	Maximum allowable canceling to stimulating current ratio
	α	Tolerable sensation interference threshold

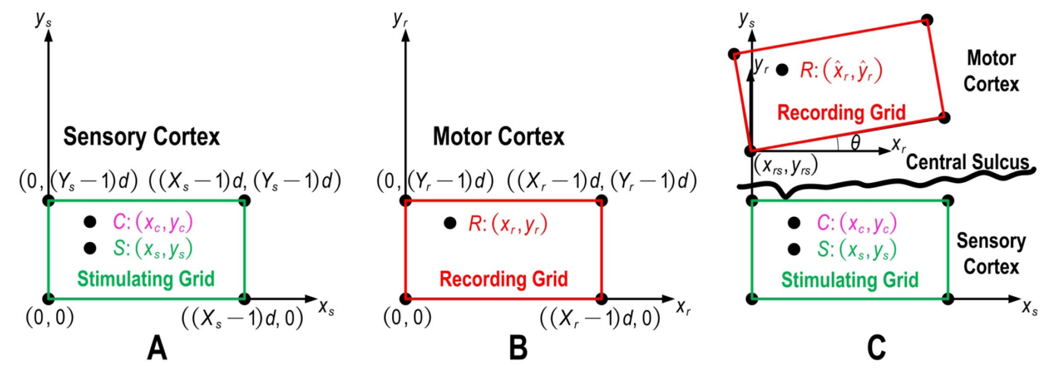

Figure C1. Physical configuration of the mathematical model. A: the location of the stimulating grid. B: the location of the recording grid. C: the stimulating and recording grids in one coordinate system to show their relative position and angle.

C as:

$$(x_c, y_c) = (p_c \cdot d, q_c \cdot d), \ \ p_c = 0, 1, \ldots, X_s - 1, \ \ q_c = 0, 1, \ldots, Y_s - 1 \tag{C2}$$

Similarly, we define the number of rows and columns of the recording grid to be Y_r and X_r, respectively, as shown in figure C1(B). Thus, a recording electrode location R is represented as:

$$(x_r, y_r) = (p_r \cdot d, q_r \cdot d), \ \ p_r = 0, 1, \ldots, X_r - 1, \ \ q_r = 0, 1, \ldots, Y_r - 1 \tag{C3}$$

The physical configuration of the model is constructed by placing the recording grid into the Cartesian coordinate system whose origin coincides with the bottom-left corner of the stimulating grid, as shown in figure C1(C), where (x_{rs}, y_{rs}) and θ are the relative position and angle, respectively. It follows readily that the recording electrode position $(\hat{x}_r, \hat{y}_r)$ in this coordinate system is:

$$\hat{x}_r = \sqrt{p_r^2 + q_r^2} \cdot d \cdot \cos\left(\arctan\left(q_r/p_r\right) + \theta\right) + x_{rs} \tag{C4}$$

$$\hat{y}_r = \sqrt{p_r^2 + q_r^2} \cdot d \cdot \sin\left(\arctan\left(q_r/p_r\right) + \theta\right) + y_{rs} \tag{C5}$$

Therefore, from geometric characterization perspective, the model needs eight model parameters, namely X_s, Y_s, X_r, Y_r, d, x_{rs}, y_{rs}, and θ, to define the location of the grids and their relative position and angle. These eight model parameters depend on clinical conditions and are predefined by clinicians.

D. Canceling dipole physical constraint *PC*

Since the canceling dipole electrodes are chosen from those on the stimulating grid, the source and sink electrode locations of all the canceling dipoles are represented as:

$$(x_{c,n}^+, y_{c,n}^+) = (p_{c,n}^+ \cdot d, q_{c,n}^+ \cdot d), \forall n = 1, 2, \ldots, N \tag{D1}$$

$$(x_{c,n}^-, y_{c,n}^-) = (p_{c,n}^- \cdot d, q_{c,n}^- \cdot d), \forall n = 1, 2, \ldots, N \tag{D2}$$

where $p_{c,n}^+, p_{c,n}^- = 0, 1, \ldots, X_s - 1$ and $q_{c,n}^+, q_{c,n}^- = 0, 1, \ldots, Y_s - 1$.

Among all the possible coordinates of the canceling dipole electrode, the first sub-constraint excludes cases wherein a canceling electrode overlaps with one of the primary stimulating electrodes, which is illustrated as:

$$(x_{c,n}^+, y_{c,n}^+) \neq (x_s^+, y_s^+), \forall n = 1, 2, \ldots, N \tag{D3}$$

$$(x_{c,n}^+, y_{c,n}^+) \neq (x_s^-, y_s^-), \forall n = 1, 2, \ldots, N \tag{D4}$$

$$(x_{c,n}^-, y_{c,n}^-) \neq (x_s^+, y_s^+), \forall n = 1, 2, \ldots, N \tag{D5}$$

$$(x_{c,n}^-, y_{c,n}^-) \neq (x_s^-, y_s^-), \forall n = 1, 2, \ldots, N \tag{D6}$$

The second sub-constraint excludes cases wherein two canceling dipoles share electrodes, which is shown as:

$$(x_{c,i}^+, y_{c,i}^+) \neq (x_{c,j}^+, y_{c,j}^+), \forall i, j = 1, 2, \ldots, N \text{ and } i \neq j \tag{D7}$$

$$(x_{c,i}^{+}, y_{c,i}^{+}) \neq (x_{c,j}^{-}, y_{c,j}^{-}), \forall i,j = 1,2,\ldots,N \text{ and } i \neq j \tag{D8}$$

$$(x_{c,i}^{-}, y_{c,i}^{-}) \neq (x_{c,j}^{+}, y_{c,j}^{+}), \forall i,j = 1,2,\ldots,N \text{ and } i \neq j \tag{D9}$$

$$(x_{c,i}^{-}, y_{c,i}^{-}) \neq (x_{c,j}^{-}, y_{c,j}^{-}), \forall i,j = 1,2,\ldots,N \\ \text{and } i \neq j \tag{D10}$$

E. Derivation of the interference function *IF*

By substituting $U_s(x,y,z)$ and $U_{c,n}(x,y,z)$, defined in appendix A, into equation (5), the activating functions due to the stimulating dipole $AF_s(x,y,z)$ and the n^{th} canceling dipole $AF_{c,n}(x,y,z)$, $n = 1, \ldots, N$, are derived to be:

$$af_s(x,y,z) = \frac{I_s}{4\pi\sigma}\left[-\frac{(r_s^{+}(x,y,z))^2 - 3z^2}{(r_s^{+}(x,y,z))^5} + \frac{(r_s^{-}(x,y,z))^2 - 3z^2}{(r_s^{-}(x,y,z))^5}\right] \tag{E1}$$

$$af_{c,n}(x,y,z) = -\frac{I_{c,n}}{4\pi\sigma}\left[-\frac{(r_{c,n}^{+}(x,y,z))^2 - 3z^2}{(r_{c,n}^{+}(x,y,z))^5} + \frac{(r_{c,n}^{-}(x,y,z))^2 - 3z^2}{(r_{c,n}^{-}(x,y,z))^5}\right] \tag{E2}$$

where r^{+} and r^{-} represent the distances from observation point (x,y,z) to dipole source and sink electrodes, respectively.

The interference constraint *IC* is based on two assumptions. First, since $af_s(x,y,z)$ reaches the maximum right beneath the two primary stimulating electrodes, we assume that the artificial sensation happens underneath the primary stimulating dipole where the interference is needed to be evaluated. Thus, (x,y) is equal to (x_s^{+}, y_s^{+}) or (x_s^{-}, y_s^{-}). To explicitly demonstrate all the variables to be optimized in the candidate solution ($\boldsymbol{cs}$), the activating functions are written as $AF_s(z)$ and $AF_{c,n}(\boldsymbol{cs}, z)$, where

$$AF_s(z) = af_s(x,y,z)|_{(x,y)=(x_s^{+},y_s^{+}) \text{ or } (x,y)=(x_s^{-},y_s^{-})} \tag{E3}$$

$$AF_{c,n}(\boldsymbol{cs}, z) = af_{c,n}(x,y,z)|_{(x,y)=(x_s^{+},y_s^{+}) \text{ or } (x,y)=(x_s^{-},y_s^{-})} \tag{E4}$$

Second, since the averaged thickness of CSF plus cortex is around 6.5 mm [28, 29], we postulate that the sensation can be predicted by the activating function along the z-axis from $z = -6.5$ mm to $z = 0$ mm. Therefore, the regions of interest we need to evaluate the interference are (x_s^{+}, y_s^{+}, z) and (x_s^{-}, y_s^{-}, z) where $z \in [-6.5, 0]$. Under the above assumptions, we introduce an interference function (*IF*) which is defined to be the absolute value of the ratio between the activating functions of the canceling currents and stimulating current, i.e.

$$IF(\boldsymbol{cs}, z) = \left|\frac{\sum_{n=1}^{N} AF_{c,n}(\boldsymbol{cs}, z)}{AF_s(z)}\right| \tag{E5}$$

IC states that, at the observation point located underneath the stimulating dipole, if *IF* is less than the tolerable interference threshold α (e.g. 0.5%), the influence of auxiliary stimulation on the artificial sensation can be neglected.

ORCID iDs

Haoran Pu https://orcid.org/0000-0002-6787-5907
Zoran Nenadic https://orcid.org/0000-0001-5569-3797

References

[1] Krucoff M O, Rahimpour S, Slutzky M W, Edgerton V R and Turner D A 2016 Enhancing nervous system recovery through neurobiologics, neural interface training and neurorehabilitation *Front. Neurosci.* **10** 584

[2] Leuthardt E C, Schalk G, Wolpaw J R, Ojemann J G and Moran D W 2004 A brain–computer interface using electrocorticographic signals in humans *J. Neural. Eng.* **1** 63–71

[3] Wang W *et al* 2013 An electrocorticographic brain interface in an individual with tetraplegia *PLoS One* **8** 1–8

[4] Benabid A L, Costecalde T, Eliseyev A, Charvet G and Verney A *et al* 2019 An exoskeleton controlled by an epidural wireless brain–machine interface in a tetraplegic patienta proof-of-concept demonstration *Lancet Neurol.* **18** 1112–22

[5] Hiremath S V, Tyler-Kabara E C, Wheeler J J, Moran D W, Gaunt R A and Collinger J L *et al* 2017 Human perception of electrical stimulation on the surface of somatosensory cortex *PLoS One* **12** 1–16

[6] Lee B, Kramer D, Salas M A, Kellis S and Brown D *et al* 2018 Engineering Artificial Somatosensation Through Cortical Stimulation in Humans *Front. Syst. Neurosci.* **12** 24

[7] Geller E B 2018 Responsive neurostimulation: Review of clinical trials and insights into focal epilepsy *Epilepsy. Behav.* **88** 11–20

[8] Wagenaar D A and Potter S M 2002 Real-time multi-channel stimulus artifact suppression by local curve fitting *J. Neurosci. Methods* **120** 113–20

[9] Sillay K A, Ondoma S, Wingeier B, Schomberg D, Sharma P and Kumar R *et al* 2018 Long-term surface electrode impedance recordings associated with gliosis for aclosed-loop neurostimulation device *Ann. Neurosci.* **25** 289–98

[10] Zhou A, Johnson B C and Muller R 2018 Toward true closed-loop neuromodulation: artifact-free recording during stimulation *Curr. Opin. Neurobiol.* **50** 119–27

[11] Mendrela A E, Cho J, Fredenburg J A, Nagaraj V, Netoff T I and Flynn M P *et al* 2016 A Bidirectional Neural Interface Circuit with Active Stimulation Artifact Cancellation and Cross-Channel Common-Mode Noise Suppression *IEEE J. Solid-State Circuits* **51** 955–65

[12] Johnson B C, Gambini S, Izyumin I, Moin A, Zhou A and Alexandrov G *et al* 2017 An implantable 700μW 64-channel neuromodulation IC for simultaneous recording and stimulation with rapid artifact recovery *Symp. VLSI Circuits* pp C48–9

[13] Cheng C, Tsai P, Yang T, Cheng W, Yen T and Luo Z *et al* 2017 A fully integrated closed-loop neuromodulation SoC

with wireless power and bi-directional data telemetry for real-time human epileptic seizure control *Symp. VLSI Circuits* pp C44–5

[14] Wang P T, McCrimmon C M, Heydari P, Do A H and Nenadic Z 2018 Subspace-based suppression of cortical stimulation artifacts *Conf. Proc. IEEE Eng. Med. Biol. Soc.* pp 2426–9

[15] Lim J, Wang P T, Pu H, Liu C Y, Kellis S, Anderson R A, Heydari P, Do A H and Nenandic Z 2019 Dipole cancellation as an artifact suppression technique in simultaneous electrocorticography stimulation and recording *Int. IEEE EMBS Conf. Neural. Eng.* pp 725–9

[16] Logothetis N K, Kayser C and Oeltermann A 2007 In vivo measurement of cortical impedance spectrum in monkeys: implications for signal propagation *Neuron* **55** 809–23

[17] Okada Y C, Huang J C, Rice M E, Tranchina D and Nicholson C 1994 Origin of the apparent tissue conductivity in the molecular and granular layers of the in vitro turtle cerebellum and the interpretation of current source-density analysis *J. Neurophysiol.* **72** 742–53

[18] Nicholson C and Freeman J A 1975 Theory of current source-density analysis and determination of conductivity tensor for anuran cerebellum *J. Neurophysiol.* **38** 356–68

[19] Ranck Jr J B 1963 Specific impedance of rabbit cerebral cortex *Exp. Neurol.* **7** 144–52

[20] Lim J, Wang P T, Shaw S J, Armacost M, Gong H and Liu C Y *et al* 2018 Artifact propagation in electrocorticography stimulation *Seventh Int. BCI Meeting, Abstract Book* pp 220–2

[21] Lim J, Wang P T, Bidhendi A K, Arasteh O M, Shaw S J and Armacost M *et al* 2018 Characterization of stimulation artifact behavior in simultaneous electrocorticography grid stimulation and recording *2018 40th Ann. Int. Conf. of the IEEE Eng. Med. Biol. Soc.* pp 4748–51

[22] Rattay F 1986 Analysis of models for external stimulation of axons *IEEE Trans. Biomed. Eng.* **BME-33** 974–7

[23] Lee C W, Dang H and Nenadic Z 2007 An efficient algorithm for current source localization with tetrodes *Conf. Proc. IEEE Eng. Med. Biol. Soc.* pp 1282–5

[24] Baumann S B, Wozny D R, Kelly S K and Meno F M 1997 The electrical conductivity of human cerebrospinal fluid at body temperature *IEEE Trans. Biomed. Eng.* **44** 220–3

[25] Rattay F 1989 Analysis of models for extracellular fiber stimulation *IEEE Trans. Biomed. Eng.* **36** 676–82

[26] Wei X F and Grill W M 2009 Analysis of high-perimeter planar electrodes for efficient neural stimulation *Front. Neuroeng.* **2** 15

[27] Guler S, Dannhauer M, Roig-Solvas B, Gkogkidis A and Macleod R *et al* 2018 Computationally optimized ECoG stimulation with local safety constraints *Neuroimage* **173** 35–48

[28] Fischl B and Dale A M 2000 Measuring the thickness of the human cerebral cortex from magnetic resonance images *Proc. Natl Acad. Sci.* **97** 11050–5

[29] Häuß inger F B, Heinzel S, Hahn T, Schecklmann M, Ehlis A C and Fallgatter A J 2011 Simulation of near-infrared light absorption considering individual head and prefrontal cortex anatomy: implications for optical neuroimaging *PLoS One* **6** 1–12

[30] Kandadai M A, Raymond J L and Shaw G J 2012 Comparison of electrical conductivities of various brain phantom gels: Developing a ’brain gel model *Mater. Sci. Eng. C: Mater. Biol. Appl.* **32** 2664–7

[31] Merrill D R, Bikson M and Jefferys J G R 2005 Electrical stimulation of excitable tissue: design of efficacious and safe protocols *J. Neurosci. Methods* **141** 171–98

[32] Sillay K A, Rutecki P, Cicora K, Worrell G, Drazkowski J and Shih J J *et al* 2013 Long-term measurement of impedance in chronically implanted depth and subdural electrodes during responsive neurostimulation in humans *Brain Stimul.* **6** 718–26

[33] Wu C, Evans J J, Skidmore C, Sperling M R and Sharan A D 2012 Impedance variations over time for a closed-loop neurostimulation device: early experience with chronically implanted electrodes *Neuromodulation* **16** 46–50

[34] Stanslaski S, Afshar P, Cong P, Giftakis J and Stypulkowski P *et al* 2012 Design and validation of a fully implantablechronicclosed-loop neuromodulation device with concurrent sensing and stimulation *IEEE Trans. Neural. Syst. Rehabil. Eng.* **20** 410–21

[35] U.S. Food and Drug Administration 2013 Neuropace RNS System: *Summary of Safety and Effectiveness Data* pp 100026

[36] Wang P T, King C E, McCrimmon C M, Lin J J, Sazgar M and Hsu F P *et al* 2016 Comparison of decoding resolution of standard and high-density electrocorticogram electrodes *J. Neural Eng.* **13** 026016